Available online at www.sciencedirect.com

ScienceDirect

Ceramics International 40 (2014) 1909–1917

CERAMICS INTERNATIONAL

www.elsevier.com/locate/ceramint

Preparation of nano-structured Ni–$Ce_{0.8}Gd_{0.2}O_{1.9}$ anode materials for solid oxide fuel cells via the water-in-oil (W/O) micro-emulsion route

Manas K. Rath[a], Mi-Jai Lee[b], Ki-Tae Lee[a,c,*]

[a]Division of Advanced Materials Engineering, Chonbuk National University, Jeonbuk 561-756, Republic of Korea
[b]Electronic Components and Materials, Korea Institute of Ceramic Engineering and Technology, Seoul 153-801, Republic of Korea
[c]Hydrogen and Fuel Cell Research Center, Chonbuk National University, Jeonbuk 561-756, Republic of Korea

Received 2 May 2013; received in revised form 2 July 2013; accepted 18 July 2013
Available online 26 July 2013

Abstract

Highly dispersed nano-crystalline NiO–$Ce_{0.8}Gd_{0.2}O_{1.9}$ (GDC) anode powders were synthesized through a novel water-in-oil (W/O) micro-emulsion route, that has not been previously reported. The spherical-shaped NiO–$Ce_{0.8}Gd_{0.2}O_{1.9}$ nano-powders exhibited a high degree of dispersion, and the morphology of the NiO–$Ce_{0.8}Gd_{0.2}O_{1.9}$ particles was controlled by varying the aqueous to oil phase ratio. The polarization resistance at 800 °C with humidified H_2 fuel and the activation energy of ME10 anode synthesized by the micro-emulsion method with the aqueous to oil phase volume ratios of 1:12 were 0.02 Ω cm^2 and 0.55 eV, respectively, which were significantly lower than those of other Ni–ceria-based anodes. These properties contributed to a smaller particle size and better dispersion compared to conventional anode materials, leading to an increased number of reaction sites. In accordance with the polarization resistance results, single cells containing ME10 anodes exhibited a high maximum power density of 0.36 W cm^{-2} at 800 °C with humidified H_2 fuel.

Keywords: Solid oxide fuel cells; Micro-emulsion; Cermet; Electrochemical performance

1. Introduction

Solid oxide fuel cells (SOFCs) are highly efficient energy conversion devices that directly convert chemical energy to electricity with varying theoretical efficiencies. A typical SOFC consists of a dense electrolyte sandwiched between two porous electrodes (an anode and a cathode) [1,2]. Currently, nickel–yttria stabilized zirconia (Ni–YSZ) cermet anodes are state-of-the-art materials for SOFC [3–7]. In general, nickel can be used in a SOFC anode due to its high electro-catalyst activity for the electrochemical oxidation of hydrogen. Nickel also has a relatively high electrical conductivity, which is necessary for optimal SOFC performances. In addition, YSZ acts as an ionic conductor, and transfers oxygen ions to the reaction site to complete the catalytic cycle.

Recently, intermediate temperature SOFCs (IT-SOFCs), which operate in the range of 500–800 °C, have garnered attention because lower temperatures minimize problems associated with thermal expansion mismatch and chemical reactivity among components. It is well known that $Ce_{0.8}Gd_{0.2}O_{1.9}$ (Gd doped ceria, GDC) has a higher ionic conductivity than YSZ at low temperatures [8,9]. In addition, GDC displays catalytic activity due to its mixed ionic-electronic conduction behavior in reducing atmospheres. Therefore, Ni–GDC cermets have been extensively investigated as anode materials for IT-SOFCs.

The performance of SOFCs depends strongly on both the microstructure of its electrodes and the intrinsic properties of its materials due to the limited electrochemical reaction that takes place at the electrolyte, gas, and anode triple-phase boundary (TPB). To improve the overall performance of SOFCs, the TPB length can be extended by tailoring the

---

*Corresponding author at: Division of Advanced Materials Engineering, Chonbuk National University, Jeonbuk 561-756, Republic of Korea. Tel.: +82 63 270 2290; fax: +82 63 270 2386.
E-mail address: ktlee71@jbnu.ac.kr (K.-T. Lee).

0272-8842/$ - see front matter © 2013 Elsevier Ltd and Techna Group S.r.l. All rights reserved.
http://dx.doi.org/10.1016/j.ceramint.2013.07.098

anode morphology. Nano-structured anode powders offer a high specific surface area, which increases the number of reaction sites. Various synthetic routes can be implemented to obtain nano-crystalline anode powders, including co-precipitation, sol–gel, combustion, hydrothermal, mechano-chemical, and emulsion methods [8–17]. Among these methods, micro-emulsion techniques are unique due to the variety of micellar structures that can be obtained, ranging from simple droplets to complex cubic compositions. The thermodynamic stability of micro-emulsions can be used to improve the formulation stability and to synthesize various compounds consisting of highly dispersed nano-participles with tailored morphologies. Moreover, low-energy mixing equipment may be used to prepare micro-emulsions [18–21]. Despite numerous investigations on the synthesis of single-component compounds such as NiO and YSZ micro-emulsions, the preparation of NiO–GDC powders with micro-emulsion method are scarce in the literature, and systematic investigations of factors that control their electro-catalytic activity towards anode reactions are rare. Thus, we present herein the synthesis of nano-structured NiO–GDC powders, the morphology of which can be tailored by controlling the water-in-oil (W/O) micro-emulsion process. We characterized the electrochemical performance of the obtained nano-structured NiO–GDC powders, and correlated their morphology with the electrochemical performance.

2. Experimental procedures

Nano-crystalline NiO–GDC cermet anode powders were synthesized by a simple water-in-oil (W/O) micro-emulsion route using $Ni(NO_3)_2 \cdot 6H_2O$ (Alfa Aesar, 98%), $Ce(NO_3)_3 \cdot 6H_2O$ (Aldrich, 99% metal basis), $Gd(NO_3)_3 \cdot xH_2O$ ($x \sim 6$, Alfa Aesar, 99.9%, REO), cyclohexane (C_6H_{12}, Alfa Aesar, 99+%), Triton®X-100 ($C_{14}H_{22}O(C_2H_4O)_n$, Alfa-Aesar), pentanol ($C_5H_{12}O$, Alfa Aesar, 98+%), NaOH (Samchun chemicals, 98.0%), and acetone (Samchun chemicals, 99.5%). De-ionized water was used for the aqueous phase. A detailed description of the synthetic procedure for the micro-emulsion is provided in Fig. 1. Three types of NiO–GDC micro-emulsions were prepared by changing the volume ratio of the aqueous (W) to oil (O) phases (W:O = 1:12, 2:12, and 3:12) and were designated ME10, ME20 and ME30, respectively.

The nano-crystalline NiO–GDC anode powders were characterized by X-ray diffraction (XRD) using Cu-Kα radiation. The morphology of the powders was evaluated by transmission electron microscopy (TEM, JEM-2010, JEOL, Japan). The BET surface area of the powders was measured with a surface area and pore size analyzer (Autosorb-1, Quantachrom instruments, USA). Microstructural characterization of the sintered samples was carried out using a scanning electron microscope (SEM, SN-3000 Hitachi, Japan). To verify the micro-emulsion process, thermogravimetric analysis (TGA, TA Q600, TA instruments, USA) and Fourier transform infrared spectroscopy (FT-IR, Spectrum GX, Perkin Elmer, USA) were employed. TGA was performed in air at temperatures ranging from 30 to 800 °C and a heating rate of 10 °C min^{-1}.

Electrochemical performance was evaluated with electrolyte-supported single cells. Commercial GDC powder (CGO90/10 UHSA, Fuel Cell Materials, USA) was compressed via cold isostatic pressing (CIP) and was subsequently fired at 1450 °C for 4 h to fabricate a 0.5-mm thick GDC electrolyte pellet. The $Ba_{0.5}Sr_{0.5}Co_{0.8}Fe_{0.2}O_{3-\delta}$–$Ce_{0.8}Gd_{0.2}O_{1.9}$ (50 wt%:50 wt%) cathode powder was synthesized by a previously described combustion method [22]. The anode and cathode pastes were produced by mixing the powder and binder (Heraeus V006) at a ratio of 70:30 wt% and the pastes were screen-printed on both sides of the GDC pellet to fabricate electrodes with a geometrical area of 0.49 cm^2. The anode and cathode layers were fired at 1250 °C and 1050 °C for 2 h, respectively. Prior to the electrochemical test, NiO in the anode was reduced to Ni in humidified H_2. *I–V* measurements of single cells were performed at 800 °C. A Pt mesh pushed onto the electrode with a spring-loaded alumina tube was used as the current corrector, a PYREX® glass ring was used as a seal between the single cell and the alumina tube. Humidified H_2 (~3% H_2O at 30 °C) and air were supplied as the fuel and oxidant, respectively, at a rate of 100 $cm^3\ min^{-1}$. AC impedance analysis was also carried out using a universal potentiostat with a frequency response analyzer (Bio-logic science instrument) in a three-electrode configuration under humidified H_2 at 700 °C, 750 °C, and 800 °C. Pt paste was used as a reference electrode with a geometrical area of 0.21 cm^2 on the anode side. The applied frequency ranged between 1 mHz and 1 MHz at a voltage amplitude of 10 mV.

3. Results and discussion

W/O micro-emulsions are thermodynamically stable and possess an optically isotropic dispersion of water nano-droplets in the oil phase. Aqueous droplets formed in such micro-emulsions can be implemented as nano-reactors for the formation of nano-crystalline particles with tailored morphologies. To obtain a stable micro-emulsion of the cyclohexane (C_6H_{12})–Triton®X-100+pentanol–H_2O system, we investigated a pseudo-ternary phase diagram, in which Triton®X-100 was used as a non-ionic surfactant due to its amphiphilic properties. The phase diagram of the three component system, which consisted of H_2O, Triton®X-100+pentanol, and cyclohexane (C_6H_{12}), is shown in Fig. 2. The ratio of C_6H_{12}, Triton®X-100, and pentanol was set to 100:12:11, which resulted in a stable transparent oil phase. Subsequently, a nitrate salt solution (aqueous phase) was gradually added to the oil mixture. McEvoy reported a similar stable region for the formation of micro-emulsions. [23]. In the present study, we were able to prepare stable W/O micro-emulsions between ME10 and ME30 without any evidence of phase separation.

Maintaining the weight fraction of the precursor is essential for maintaining the stability of micro-emulsions prior to treatment with NaOH, which was used as a precipitating reagent for crystal growth. Thus, FT-IR analysis of ME10 samples was carried out step-by-step to understand the mechanism of micro-emulsion formation (Fig. 3). Although peaks associated with functional groups were clearly visible due to the presence of organics oil phases, the peaks in the finger print region (500–1500 cm^{-1})

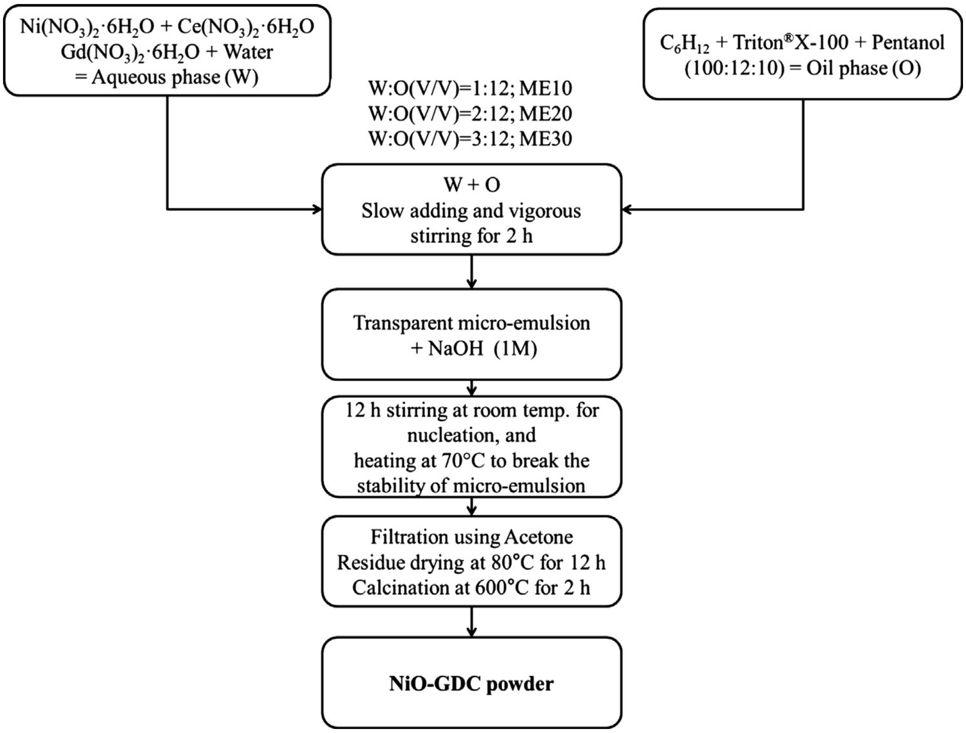

Fig. 1. Flow chart for the synthesis of nano-crystalline NiO–GDC powders using a (W/O) micro-emulsion method.

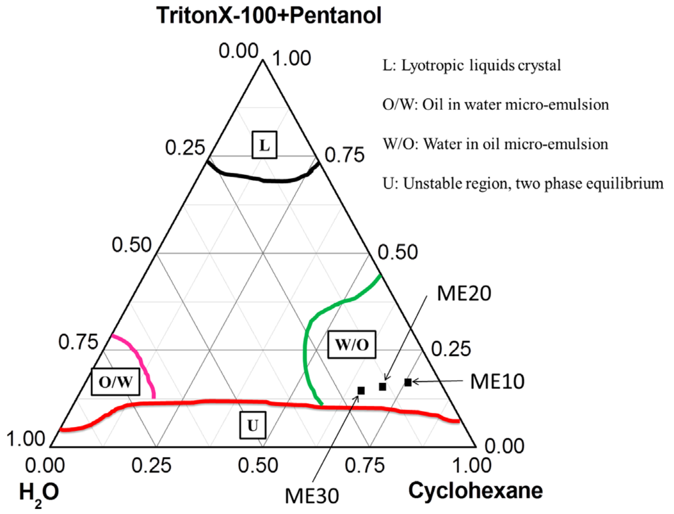

Fig. 2. Phase diagram of the three component system, which consisted of H_2O, Triton®X-100+pentanol, and cyclohexane (C_6H_{12}).

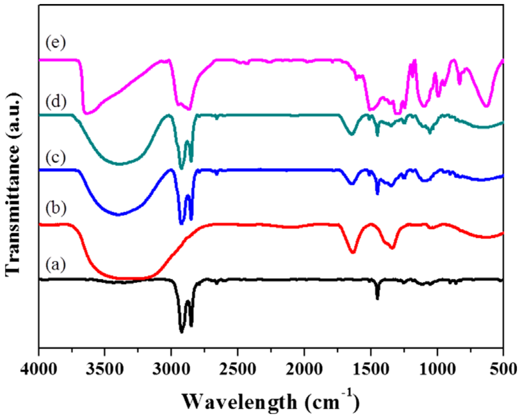

Fig. 3. FT-IR spectra of the (a) oil phase, (b) aqueous phase, (c) micro-emulsion prior to precipitation, (d) micro-emulsion after precipitation, and (e) final residue in dry form for the ME10 sample.

were very complex. Specifically, in the oil phase, the three organic solvents (cyclohexane, pentanol, and Triton®X-100) were physically mixed without any chemical reaction in the normal state; however, the surface tension, viscosity, and solubility of the mixture may have changed due to the characteristics of the surfactant and co-surfactants. The doublet at 2850 and 2927 cm^{-1} was attributed to the asymmetrical and symmetrical stretching mode of CH_2, whereas the intense peak at 1450 cm^{-1} in the finger print region was associated with C–H scissoring [24]. Several other notable peaks of low intensity were also observed, including peaks at 1050 cm^{-1}, 1188 cm^{-1}, 1128 cm^{-1}, 1456 cm^{-1}, 1512 cm^{-1}, 1610 cm^{-1}, 2660 cm^{-1}, and 279 cm^{-1}, which corresponded to primary alcohol O–H stretches, C–C stretches and C–H rocking, CH_2 twists, CH_2 wags, C–H scissoring, C–C stretches, 1st overtone of CH deformation, and C–O stretches of CHO groups, respectively [24–28]. In the aqueous solution, we observed broad peaks at 635 cm^{-1} and 3320 cm^{-1}, which corresponded to M–O and M–OH bonding vibrations and the typical H–OH stretch of H_2O, respectively. The intense peaks at 1390 cm^{-1} and 1634 cm^{-1} corresponded to the νaNO_3^- stretch of salts precursors and the in-plane deformation of δH_2O, respectively [29,30]. Because the micro-emulsion was formed by physical mixing of the aqueous and oil phases and was mediated by surfactants, forming a thermodynamically stable and transparent solution, solvents should not have reacted with each other nor changed their chemical structure during the formation of the micro-emulsion. Thus, cyclohexane, pentanol, and Triton®X-100 coexisted in the oil phase during the formation of the micro-emulsion, and served to confine the aqueous phases to generate an aqueous core. Furthermore, while the surfactant (Triton®X-100) separated the aqueous phase from the oil phase to become a semipermeable membrane, the co-surfactant (cyclohexane) enhanced the solubility limit of the aqueous phase. Therefore, if the prepared micro-emulsion was stable, one can expect the resulting FT-IR spectra to match the peaks corresponding to either an oil mixture phase or aqueous phase. As shown in Fig. 3(c), all of the peaks in the FT-IR spectra of ME10 matched those of the oil and aqueous phases in Fig. 3(a) and (b), respectively. However, the peak corresponding to the in-plane deformation of δH_2O at 1643 cm^{-1} exhibited a red-shift after micro-emulsion formation due to the surface absorption of the surfactant terminal [26]. Conversely, the peak at 1350 cm^{-1} corresponding to the νaNO_3^- stretch exhibited a blue-shift, which was attributed to coagulation of the aqueous core containing NO_3^- species along with precursor metal ions [31]. Although significant differences were not detected in the spectra of NiO–GDC micro-emulsions before and after precipitation, we did observe several changes with respect to the peak intensity and generation of new peaks. Specifically, we observed a new shoulder peak at 2957 cm^{-1} corresponding to the sp^3 C–H stretches near the doublet of CH_2 asymmetric and symmetric stretches [25]. The appearance of this spectral line was due to the transformation of the carbon atom from sp^2 to sp^3 hybridization. Meanwhile, the peaks at 1050 cm^{-1} and 1258 cm^{-1} corresponding to the primary alcohol O–H stretches and C–O bending became more intense and distinct, which may be due to an increase in the pH and subsequent phase separation in the micro-emulsion. Fig. 3(e) shows the FT-IR spectra of a dry residue composed of an amorphous NiO, GDC, and hydroxide phase of the metal containing organic residues. A sharp peak at 3654 cm^{-1} was observed and was attributed to non-hydrogen bonded O–H groups corresponding to β-$Ni(OH)_2$ [31,32]. All of the peaks between 1500 cm^{-1} and 3000 cm^{-1} corresponded to the vibrational modes of the functional groups of organic residues [33]. In addition, the intense peaks at 480 cm^{-1} and 627 cm^{-1} corresponded to the Ni–O stretch and the phonon band of δCe–O-C or δNi–O–H vibrations, respectively [31–35].

TGA plots of micro-emulsion mediated NiO–GDC precipitates pre-calcined at 300 °C for 6 h are shown in Fig. 4. The pre-calcination process was carried out prior to TGA because composition effects due to weight losses greater than 85% are difficult to detect for organic components without the application of a pre-calcination process. Two major forms of weight loss were distinctly visible in the TGA plots. The first weight loss occurred between room temperature and approximately 300 °C and was due to the loss of water and organic components that remained after pre-calcination. The weight losses for ME10, ME20 and ME30 were 1.95%, 2.02%, and 2.39%, respectively. According to TGA, the amount of the first weight loss was proportional to the aqueous phase of the micro-emulsion. However, the second weight loss for ME10, ME20 and ME30 occurred between 300 °C and 600 °C and was 3.33%, 4.21%, and 4.50%, respectively. The second weight loss series corresponded to the decomposition of $Ni(OH)_2$ to NiO, $Ce(OH)_4$ to CeO_2, and $Gd(OH)_3$ to Gd_2O_3. Therefore, a high aqueous to oil phase ratio in the micro-emulsions, which corresponded to an increased abundance of Ni, Ce, and Gd micelles, resulted in increased weight loss. The TGA data also revealed that a calcination temperature of greater than 600 °C should be used to obtain pure NiO–GDC powders.

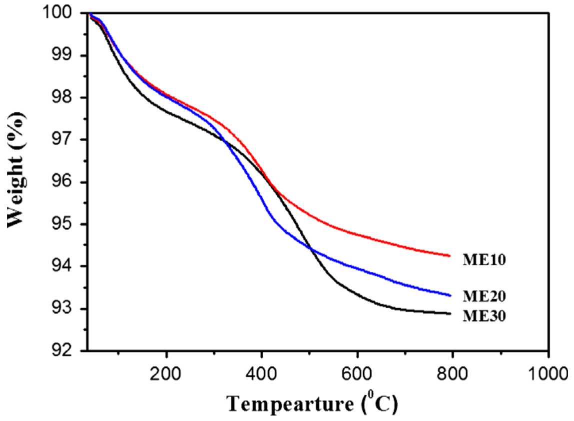

Fig. 4. TGA data for NiO–GDC precipitates pre-calcined at 300 °C for 6 h.

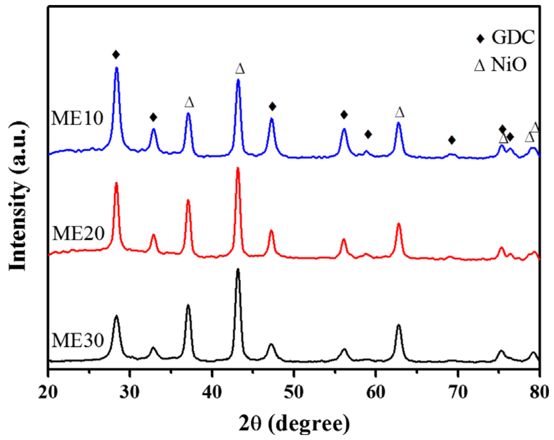

Fig. 5. XRD patterns of NiO–GDC powders calcined at 600 °C for 2 h.

The XRD patterns of NiO–GDC powders calcined at 600 °C for 2 h are shown in Fig. 5. All of the NiO–GDC powders exhibited a single phase without any secondary phases or impurity phases, and all of the peaks matched that of cubic NiO (Fm3m, JCPDF #47–1049) and cubic $Ce_{0.8}Gd_{0.2}O_{1.9}$ (Fm3m, JCPDF #34–0394). According to the Scherrer's formula, the calculated mean crystallite sizes of NiO for ME10, ME20, and ME30 NiO–GDC powders were 13.2 mm, 14.8 nm, and 13.4 nm, while those of GDC were 11.7 nm, 13.7 nm, and 10.6 nm, respectively. It has been reported that crystallite sizes of NiO and GDC in NiO–GDC synthesized by direct thermal treatment of a polymeric sol–gel at 800 °C for 2 h was 24 nm and 18 nm, respectively [36].

Ding et al. reported that NiO and GDC have 30.5 nm and 27.3 nm of crystallite size in the NiO–GDC composite powders synthesized by a hydroxide co-precipitation method [37]. Similarly, Wandekar et al. also reported that NiO–GDC powders prepared by solution combustion synthesis consisted of 30–58 nm sized NiO and 40–50 nm sized GDC [38]. Interestingly, NiO–GDC powders synthesized by the micro-emulsion method showed smaller crystallite size than those prepared by other synthesis methods.

Although significant differences in the crystallite size were not observed, the overall morphology of the NiO–GDC powders was dependent on the aqueous to oil phase ratio, as shown in Fig. 6. The particle size of spherical NiO–GDC powders, which ranged from 12 to 20 nm, increased with an increase in the aqueous to oil phase ratio (ME10 < ∩ ME20 < ME30). Meanwhile, the ME10 powder with the lowest aqueous to oil phase ratio exhibited the highest degree of dispersion compared to the other powders, which may be due to the relatively low concentration of micelles. However, further reactions in the aqueous to oil phase ratio were difficult to achieve due to yield losses. Thus, a trade-off between the powder quality and yield may be necessary to identify the optimal composition of the micro-emulsion process.

Unlike the particle size, the surface area of NiO–GDC powders decreased with an increase in the aqueous to oil phase ratio. Specifically, the BET surface areas of ME10, ME20, and ME30 anode powders were 16.8 $m^2 g^{-1}$, 12.9 $m^2 g^{-1}$, and 8.4 $m^2 g^{-1}$, respectively. Considering that the catalytic reaction occurs on the anode surface, one may expect that the ME10 anode with the largest surface area should exhibit the best electrochemical performance.

The AC impedance spectra of Ni–GDC anodes in humidified H_2 are shown in Fig. 7. An equivalent circuit consisting of an inductor (L), a resistor (R_o), and two RQ elements (R_1Q_1 and R_2Q_2) were used to fit the impedance data, as described in Fig. 7 (a). The left intercept with the impedance semi-circle on the Z_{re} axis at high frequencies indicates the ohmic resistance, R_o, while the right intercept on the Z_{re} axis corresponds to the total resistance, R_{tot}. The polarization resistance, R_p, is the overall size of the arcs ($R_{tot} - R_o$). The calculated R_p values at 700 °C, 750 °C, and 800 °C are listed in Table 1. The R_p value at a given temperature in H_2 increased linearly as the aqueous to oil phase ratio increased. Considering the TPB length, one would expect that ME10 anodes with small particle sizes and high degrees of dispersion would exhibit the best electrochemical performance, as shown in Fig. 6. It has been reported that the polarization resistance of Ni–GDC anode synthesized by GNP method was 0.06 $\Omega\,cm^2$ at 600 °C under humidified H_2 with GDC electrolyte supported cell [39]. Recently, Choi et al. also reported that the polarization resistance value of the Ni–GDC anode supported cell at 650 °C is about 0.40 $\Omega\,cm^2$ [40]. Although it is hard to compare the polarization resistance values of various Ni–GDC anodes directly due to a difference in the cell configuration, the electro-catalytic activity of the Ni–GDC anode synthesized by the micro-emulsion method could be comparable to that of other Ni–GDC anodes synthesized by various solution based methods.

The temperature dependencies of the ohmic (R_o) and polarization (R_p) resistances are shown in Fig. 8, and the calculated activation energies, E_a, are provided in Table 1. The activation energy of the Ni–GDC anode synthesized in the present study by the proposed micro-emulsion method was significantly lower than that of previously investigated Ni–ceria-based anodes. As previously reported, the activation energy of Ni–GDC anodes prepared by impregnation is 0.91 eV at temperatures of 700–1000 °C [41]. Similarly, Muecke et al. reported that nano-crystalline Ni–GDC thin film anodes have an activation energy of 1.45 eV at a temperatures of 400–600 °C [42], while Wang et al. reported an activation energy value of 1.01 eV for Ni–$Sm_{0.15}Ce_{0.85}O_{2-\delta}$ anodes at temperatures of 600–800 °C [43].

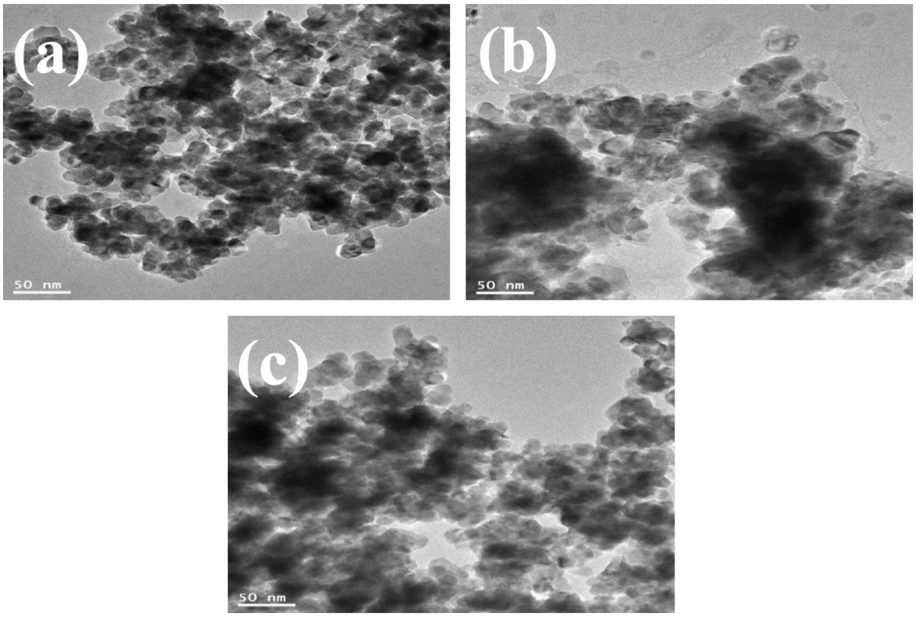

Fig. 6. TEM micrographs of NiO–GDC powders calcined at 600 °C for 2 h of (a) ME10, (b) ME20, and (c) ME30.

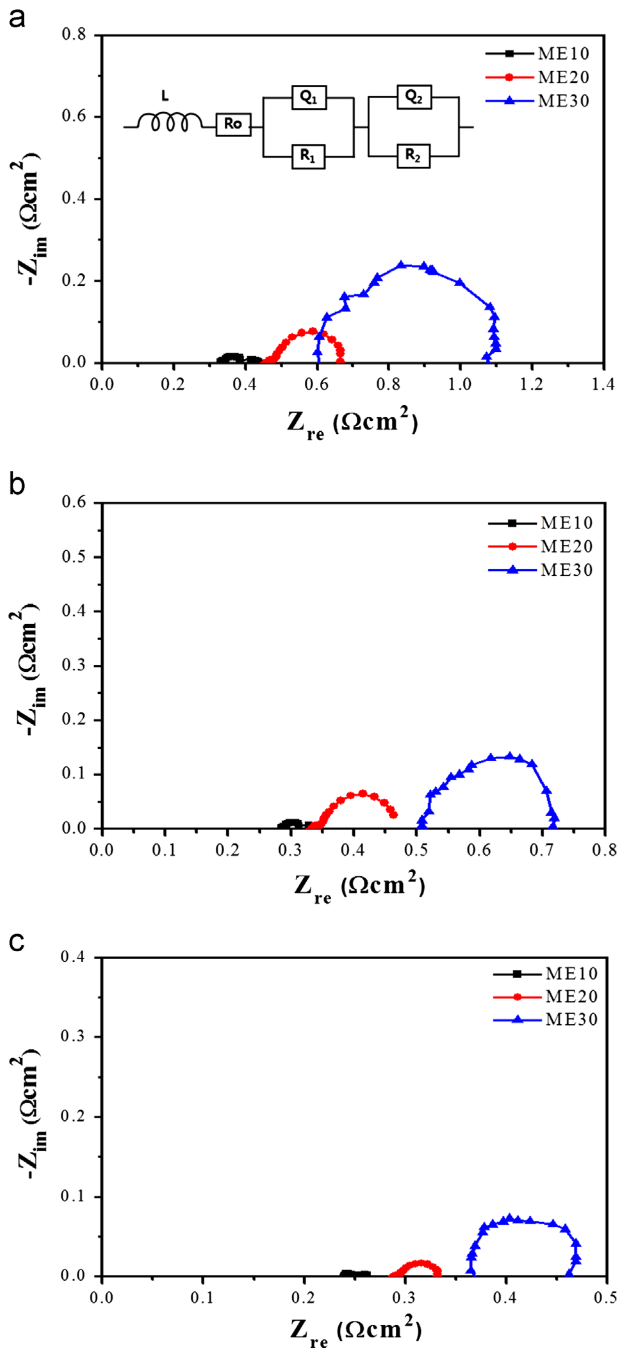

Fig. 7. Typical AC impedance spectra of Ni–GDC anodes at (a) 700 °C, (b) 750 °C, and (c) 800 °C in humidified H_2.

Table 1
Polarization resistance and activation energy of Ni–GDC anodes at various operating temperatures in humidified H_2.

Anode material	Polarization resistance (Ω cm^2)			Activation energy (eV)
	700 °C	750 °C	800 °C	
ME10	0.095	0.047	0.021	0.55
ME20	0.217	0.137	0.054	0.58
ME30	0.464	0.216	0.110	0.61

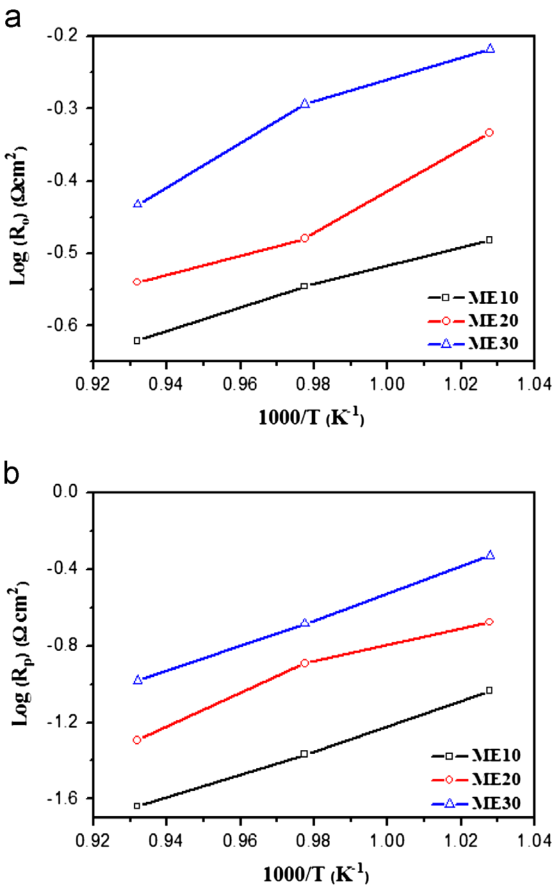

Fig. 8. Temperature dependence of the (a) ohmic (R_o) and (b) polarization (R_p) resistances of Ni–GDC anodes in humidified H_2.

Meanwhile, the total polarization resistance (R_p) was separated by R_1 and R_2 which correspond to the high-frequency semi-circle and the low-frequency semi-circle, respectively, to verify the individual electrode reaction processes. The separated polarization resistance values for the composite anodes in humidified H_2 atmosphere are listed in Table 2. The ME10 anode showed the lowest R_1 and R_2 values. Interestingly, the R_1 value is lower than the R_2 value for all the compositions. Nakagawa et al. reported that the semi-circle on the high-frequency side (R_1) corresponded to the activation process and that the semi-circle at the low-frequency side (R_2) corresponded to the diffusion process [44]. Therefore, the diffusion process could be the rate-determining step for the Ni–GDC anode synthesized by micro-emulsion method. Meanwhile, the R_1 value of ME10 anode was significantly lower than those of ME20 and ME30 at 800 °C. Since the oxidation reaction of fuel at the anode side is strongly affected by the electrode microstructure, which restrains the reaction sites such as TPB, the ME10 anode with the smaller grain size and the better-distributed pore structure, as shown in Fig. 9, exhibits the lowest R_1 value.

Fig. 9 compares the SEM micrographs of Ni–GDC anodes synthesized by the proposed micro-emulsion method after the electrochemical performance test. The grain size of the anodes

Table 2
The separated polarization resistance values for the composite anodes humidified H_2.

Anode material	Temperature (°C)	Polarization resistance (Ω cm^2)	
		R_1	R_2
ME10	700	0.045	0.050
	750	0.007	0.040
	800	0.003	0.018
ME20	700	0.105	0.112
	750	0.051	0.086
	800	0.025	0.029
ME30	700	0.120	0.344
	750	0.081	0.135
	800	0.049	0.061

increased with an increase in the aqueous to oil phase ratio (ME10 < ME20 < ME30), suggesting that highly dispersed GDC particles may block the grain growth of Ni particles. Moreover, compared with ME20 and the ME30 anodes, the ME10 anode exhibited a porous structure with meso- and micro-pores, suggesting that the TPB area was enlarged throughout the porous anode structure compared to that of the other anodes. The observed differences in the microstructures of sintered anodes may have been induced by the initial morphology of the powders as evidenced in Fig. 6 and the BET analysis.

The cell voltages and power densities of Ni–GDC anodes synthesized by the proposed micro-emulsion method are shown in Fig. 10. The open circuit voltages at 800 °C were 0.76 ± 0.02 V. The relatively low open circuit voltage could mainly be due to the reduction of GDC electrolytes in a reducing atmosphere rather than gas leakage. Zha et al. calculated theoretical electromotive force (EMF) of a SOFC based on fluorite structure electrolyte such as YSZ and GDC by defect chemistry analysis [45]. In case of GDC ($Ce_{0.8}Gd_{0.2}O_{1.9}$), the calculated EMF value was 0.85 V at 800 °C with 3%H_2O–H_2 gas at anode side and pure O_2 gas at cathode side [45]. The open circuit voltage of 0.76 V at 800 °C in this study could be reasonable value considering air atmosphere at the cathode side. It has been also reported that the open circuit voltage of single cell with GDC electrolyte was 0.77 V at 800 °C with a mixture of 1.5%H_2O–H_2 and air as fuel and oxidant gases, respectively [46]. Meanwhile, the open circuit voltage depends on the thickness of a mixed conducting electrolyte such as doped ceria. Duncan et al. reported that the open circuit voltage of Ni–GDC/GDC/LSCF–GDC cell increased with an increase in the thickness of GDC electrolyte and then saturated around 100 μm [47]. Therefore, a 500-μm thick GDC electrolyte may not affect the open circuit voltage in this study. The maximum power density of a single cell containing the ME10 anode was 0.36 W cm^{-2}, which was higher than that of single cells containing ME20 and ME30 anodes. The observed changes in the power density in a humidified H_2 atmosphere due to changes in the aqueous to oil phase ratio were consistent with the general trends in the AC impedance data. Although Ni–GDC anodes synthesized by the proposed micro-emulsion method exhibited relatively improved electrochemical performance compared to that of other conventional anode materials, the overall electrochemical performance of the single cell was relatively poor, which was attributed to the use of a 500-μm thick electrolyte. Further studies using an ultra-thin electrolyte may be beneficial, considering the ohmic resistance of the electrolyte. In addition, if the operation of the $Ba_{0.5}Sr_{0.5}Co_{0.8}Fe_{0.2}O_{3-\delta}$–$Ce_{0.8}Gd_{0.2}O_{1.9}$ cathode is optimized, the electrochemical performance may be further improved.

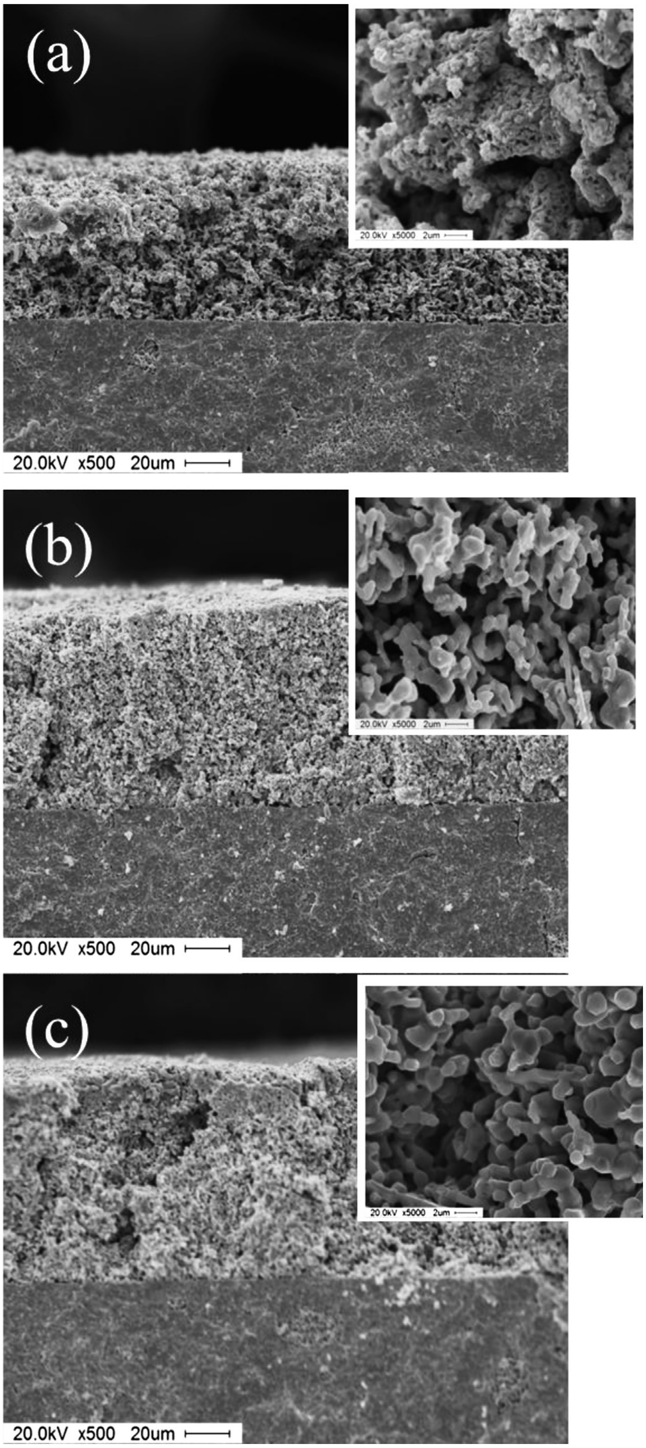

Fig. 9. SEM micrographs of NiO–GDC anodes of (a) ME10, (b) ME20, and (c) ME30 fired at 1250 °C for 2 h. The inset shows an enlarged micrograph of the anode region.

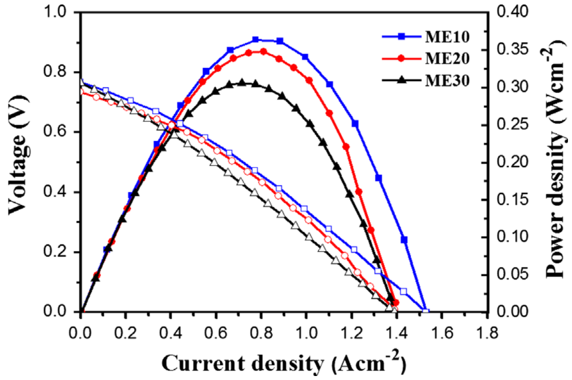

Fig. 10. Comparison of *I–V* curves (open symbols) and power densities (closed symbols) of Ni–GDC anodes at 800 °C.

4. Conclusions

NiO–GDC cermet powders without any impurities were successfully synthesized by a water-in-oil (W/O) micro-emulsion route. The nano-sized powders possessed a spherical shape with a high degree of dispersion. The morphology of the powders was controlled by varying the synthetic conditions, including the aqueous to oil phase ratio. However, during the optimization of the micro-emulsion process, a trade-off between the powder quality and yield was observed. The polarization resistance and activation energy of the Ni–GDC anodes synthesized in the present study by the proposed micro-emulsion method were significantly lower than those of conventional Ni–ceria-based anodes due to the enlarged TPB area. The single cell containing an ME10 anode exhibited a maximum power density of 0.36 W cm^{-2}. Thus, the water-in-oil (W/O) micro-emulsion method, which can be used to control the nano-structure and powder morphology, may be useful for the preparation of SOFC electrode materials.

Acknowledgments

This research was supported by the Basic Science Research Program through the National Research Foundation of Korea (NRF) funded by the Ministry of Education, Science and Technology (Grant no.: 2010-0009130). This work was also supported by a Human Resources Development of the Korea Institute of Energy Technology Evaluation and Planning (KETEP) grant funded by the Korean government Ministry of Knowledge Economy (No. 20114030200060).

References

[1] N.Q. Minh, Ceramic fuel cells, Journal of the American Ceramic Society 76 (1993) 563–588.

[2] S.C. Singhal, Advances in solid oxide fuel cell technology, Solid State Ionics 135 (2000) 305–313.

[3] S.D. Kim, H. Moon, S.H. Hyun, J. Moon, J. Kim, H.W. Lee, Performance and durability of Ni-coated YSZ anodes for intermediate temperature solid oxide fuel cells, Solid State Ionics 177 (2006) 931–938.

[4] H. Koide, Y. Someya, T. Yoshida, T. Maruyama, Properties of Ni/YSZ cermet as anode for SOFC, Solid State Ionics 132 (2000) 253–260.

[5] M. Marinsek, K. Zupan, J. Macek, Preparation of Ni–YSZ composite materials for solid oxide fuel cell anodes by the gel-precipitation method, Journal of Power Sources 86 (2000) 383–389.

[6] S.P. Jiang, P.J. Callus, S.P.S. Badwal, Fabrication and performance of Ni/3 mol% Y_2O_3–ZrO_2 cermet anodes for solid oxide fuel cells, Solid State Ionics 132 (2000) 1–14.

[7] H.J. Cho, G.M. Choi, Effect of milling methods on performance of Ni–Y_2O_3-stabilized ZrO_2 anode for solid oxide fuel cell, Journal of Power Sources 176 (2008) 96–101.

[8] C. Ding, H. Lin, K. Sato, T. Kawada, J. Mizusaki, T. Hashida, Improvement of electrochemical performance of anode-supported SOFCs by NiO–$Ce_{0.9}Gd_{0.1}O_{1.95}$ nanocomposite powders, Solid State Ionics 181 (2010) 1238–1243.

[9] C. Ding, K. Sato, J. Mizusaki, T. Hashida, A comparative study of NiO–$Ce_{0.9}Gd_{0.1}O_{1.95}$ nanocomposite powders synthesized by hydroxide and oxalate co-precipitation methods, Ceramics International (2012) 85–92.

[10] C. Ding, H. Lin, K. Sato, T. Hashida, Synthesis of NiO–$Ce_{0.9}Gd_{0.1}O_{1.95}$ nanocomposite powders for low-temperature solid oxide fuel cell anodes by co-precipitation, Scripta Materialia 60 (2009) 254–256.

[11] J.S. Lian, X.Y. Zhang, H.P. Zhang, Z.H. Jiang, J. Zhang, Synthesis of nanocrystalline NiO/doped CeO_2 compound powders through combustion of citrate/nitrate gel, Materials Letters 58 (2004) 1183–1188.

[12] C. Xia, M. Liu, Microstructures, conductivities, and electrochemical properties of $Ce_{0.9}Gd_{0.1}O_2$ and GDC–Ni anodes for low-temperature SOFCs, Solid State Ionics 152–153 (2002) 423–430.

[13] A.A. Fakhrabadi, R.E. Avila, H.E. Carrasco, S. Ananthakumar, R. V. Mangalaraja, Combustion synthesis of NiO–$Ce_{0.9}Gd_{0.1}O_{1.95}$ nanocomposite anode and its electrical characteristics of semi-cell configured SOFC assembly, Journal of Alloys and Compounds 541 (2012) 1–5.

[14] W. Huang, P. Shuk, M. Greenblatt, Properties of sol-gel prepared $Ce_{1-x}Sm_xO_{2-x/2}$ solid electrolytes, Solid State Ionics 100 (1997) 23–27.

[15] J.M. Lim, S.W. Kim, Synthesis of nickel coated gadolinia doped ceria nanopowder by microwave radiation, Materials Science Forum 569 (2008) 77–80.

[16] T. Misono, K. Murata, J. Yin, T. Fukui, Morphology control of Ni–GDC cermet anode for lower temperature SOFC, ECS Transactions 7 (1) (2007) 1355–1361.

[17] S.P. Jiang, S.H. Chan, A review of anode materials development in solid oxide fuel cells, Journal of Materials Science 29 (2004) 4405–4439.

[18] A.K. Ganguli, T. Ahmad, S. Vaidya, J. Ahmed, Microemulsion route to the synthesis of nanoparticles, Pure and Applied Chemistry 80 (2008) 2451–2477.

[19] M.P. Pileni, Reverse micelles used as templates: a new understanding in nanocrystal growth, Journal of Experimental Nanoscience 1 (2006) 13–27.

[20] M.A. López-Quintela, Synthesis of nanomaterials in microemulsions: formation mechanisms and growth control, Current Opinion in Colloid and Interface Science 8 (2003) 137–144.

[21] B.K. Paul, S.P. Moulik, Uses and applications of microemulsions, Current Science (2001) 990–1001.

[22] M.K. Rath, B.H. Choi, K.T. Lee, Properties and electrochemical performance of $La_{0.75}Sr_{0.25}Cr_{0.5}Mn_{0.5}O_{3-\delta}$–$La_{0.2}Ce_{0.8}O_{2-\delta}$ composite anodes for solid oxide fuel cells, Journal of Power Sources 213 (2012) 55–62.

[23] E. McEvoy, The Development and Application of Oil-in-Water Micro-emulsion Liquids and Electrokinetic Chromatography for Pharmaceutical Analysis, Waterford Institute of Technology, Ireland, 2008 (Doctoral degree thesis).

[24] R.A. Nyquist, C.L. Putzig, Handbook of Infrared and Raman Spectra of Inorganic Compounds and Organic, Academic Press Inc., San Diago, CA, USA, 1990.

[25] J. Cates, in: R.A. Mayers (Ed.), Encyclopaedia of Analytical Chemistry, John Wiley & Sons Ltd., Chichester, 2002, pp. 10815–10837.

[26] R. Pramanik, S. Sarkar, C. Ghatak, V.G. Rao, P. Setua, N. Sarkar, Microemulsions with surfactant TX100, cyclohexane, and an ionic liquid investigated by conductance, DLS, FTIR measurements, and study of solvent and rotational relaxation within this microemulsion, Journal of Physical Chemistry B 114 (2010) 7579–7586.

[27] N. Kimura, J. Umemura, S. Hayashi, Polarized FT-IR spectra of water in the middle phase of Triton X100-water system, Journal of Colloid and Interface Science 182 (1996) 356–364.

[28] S.M. Barnett, S. Dracheva, R.W. Hendler, I.W. Levin, Lipid-induced conformational changes of an integral membrane protein: an infrared spectroscopic study of the effects of Triton X-100 treatment on the purple membrane of halobacterium halobium ET1001, Biochemistry 35 (1996) 4558–4567.

[29] J. Ryczkowski, IR spectroscopy in catalysis, Catalysis Today 68 (2001) 263–381.

[30] M. Taibi, S. Ammar, N. Jouini, F. Fiévet, P. Molinié, M. Drillon, Layered nickel hydroxide salts: synthesis, characterization and magnetic behaviour in relation to the basal spacing, Journal of Materials Chemistry 12 (2002) 3238–3244.

[31] T.N. Ramesh, P.V. Kamath, Synthesis of nickel hydroxide: effect of precipitation conditions on phase selectivity and structural disorder, Journal of Power Sources 156 (2006) 655–661.

[32] Y. Khan, S.K. Durrani, M. Mehmood, A. Jan, M.A. Abbasi, pH-dependant structural and morphology evolution of $Ni(OH)_2$ nanostructures and their morphology retention upon thermal annealing to NiO, Materials Chemistry and Physics 130 (2011) 1169–1174.

[33] M. Zawadzki, Preparation and characterization of ceria nanoparticles by microwave-assisted solvothermal process, Journal of Alloys and Compounds 454 (2008) 347–351.

[34] P.V. Kamath, G.N. Subbanna, Electroless nickel hydroxide: synthesis and characterization, Journal of Applied Electrochemistry 22 (1992) 478–482.

[35] M.L.D. Santos, R.C. Lima, C.S. Riccardi, R.L. Tranquilin, P.R. Bueno, J.A. Varela, E. Longo, Preparation and characterization of ceria nanospheres by microwave-hydrothermal method, Materials Letters 62 (2008) 4509–4511.

[36] D.A. Macedo, G.L. Souza, B. Celac, C.A. Paskocimas, A.E. Martinelli, F.M.L. Figueiredo, F.M.B. Marques, R.M. Nascimento, A versatile route for the preparation of Ni–CGO cermets from nanocomposite powders, Ceramics International 39 (2013) 4321–4328.

[37] C. Ding, H. Lin, K. Sato, T. Hashida, Synthesis of NiO–$Ce_{0.9}Gd_{0.1}O_{1.95}$ nanocomposite powders for low-temperature solid oxide fuel cell anodes by co-precipitation, Scripta Materialia 60 (2009) 254–256.

[38] R.V. Wandekar, M. Ali (Basu), B.N. Wani, S.R. Bharadwaj, Physico-chemical studies of NiO–GDC composites, Materials Chemistry and Physics 99 (2006) 289–294.

[39] S. Zha, W. Rauch, M. Liu, Ni–$Ce_{0.9}Gd_{0.1}O_{1.95}$ anode for GDC electrolyte-based low-temperature SOFCs, Solid State Ionics 166 (2004) 241–250.

[40] Y.G. Choi, J.Y. Park, H. Song, H.R. Kim, J.W. Son, J.H. Lee, H.J. Je, B.K. Kim, H.W. Lee, K.J. Yoon, Microstructure–polarization relations in nickel/gadolinia-doped ceria anode for intermediate-temperature solid oxide fuel cells, Ceramics International 39 (2013) 4713–4718.

[41] S. Primdahl, Y.L. Liu, Ni catalyst for hydrogen conversion in gadolinia-doped ceria anodes for solid oxide fuel cells, Journal of the Electrochemical Society 149 (2002) A1466–A1472.

[42] U.P. Muecke, K. Akiba, A. Infortuna, T. Salkus, N.V. Stus, L.J. Gauckler, Electrochemical performance of nanocrystalline nickel/gadolinia-doped ceria thin film anodes for solid oxide fuel cells, Solid State Ionics 178 (2008) 1762–1768.

[43] S. Wang, M. Ando, T. Ishihara, Y. Takita, High performance Ni–$Sm_{0.15}Ce_{0.85}O_{2-\delta}$ cermet anodes for intermediate temperature solid oxide fuel cells using $LaGaO_3$ based oxide electrolytes, Solid State Ionics 174 (2004) 49–55.

[44] N. Nakagawa, H. Sakurai, K. Kondo, T. Morimoto, K. Hatanaka, K. Kato, Evaluation of the effective reaction zone at Ni(NiO)/zirconia anode by using an electrode with a novel structure, Journal of the Electrochemical Society 142 (1995) 3474–3479.

[45] S.W. Zha, C.R. Xia, G.Y. Meng, Calculation of the e.m.f. of solid oxide fuel cells, Journal of Applied Electrochemistry 31 (2001) 93–98.

[46] N. Kim, B. Kim, D. Lee, Effect of co-dopant addition on properties of gadolinia-doped ceria electrolyte, Journal of Power Sources 90 (2000) 139–143.

[47] K.L. Duncan, K.T. Lee, E.D. Wachsman, Dependence of open-circuit potential and power density on electrolyte thickness in solid oxide fuel cells with mixed conducting electrolytes, Journal of Power Sources 196 (2011) 2445–2451.